https://doi.org/10.5194/egusphere-2025-3563
Preprint. Discussion started: 16 September 2025
© Author(s) 2025. CC BY 4.0 License.

A coastal geodetic GNSS station for tectonic and sea-level variation study in the South China Sea

Qiang Qiu[1, 2], Linlin Li[3,4], Mai Ye[2], Hongqiang Yang[2,5], Xingyu Song[2,5], Tingting Zheng[1, 2], Jinghe Cao[1, 2], Peitao Wang[6], Zhanying Chen[1, 2], Zhiwen Zhang[1, 2], Kuilin Xiao[1, 2], Xing Huang[1, 2], Yadong Huang[1,5], Chuanyang Zheng[2, 5], Zhiyuan OuYang[2, 5], Xiaoming Fu[2, 5], Muzhong Wang[2], Zhen Wang[2,5], Zitao Zhang[2,5], Haiping Cui[2,5]

[1]State Key Laboratory of Tropical Oceanography, South China Sea Institute of Oceanology, Chinese Academy of Sciences, Guangzhou 510301, China

[2]Laboratory of Ocean and Marginal Sea Geology, South China Sea Institute of Oceanology, Chinese Academy of Sciences, Guangzhou 510301, China

[3]School of Earth Science and Engineering, Sun Yat-Sen University, Zhuhai 519082, China

[4]Southern Marine Science and Engineering Guangdong Laboratory (Zhuhai), Zhuhai 519082, China

[5]Nansha Marine Ecological and Environmental Research Station, Chinese Academy of Sciences, Sansha 573299, China

[6]Key Laboratory of Marine Hazards Forecasting, National Marine Environmental Forecasting Center, Ministry of Natural Resources, Beijing, China

Corresponding to: Qiang Qiu (qiu.qiang@scsio.ac.cn)

Abstract

South China Sea (SCS) separates the land from north to south by nearly two-thousand km in distance. In this framework, land-based observation is limited, thus, little is known about the tectonics in this widely gapped area. Here, we present a coastal geodetic GNSS station that is recently deployed in Nansha southern SCS. The station measures mm precision of land displacements that show ~4-5 mm range of variation in horizontal components and ~1 cm range of changes in vertical nearly a year. These displacements are characterized by a flat trend, with occasionally disturbed by subcentimeter changes. The GNSS-IR retrieved sea-level variations over both short- and long-term time span are comparable with tide gauge recordings, offering a complement equipment to detect amplitude variations and trend adjustments in both relative and absolute sea levels. Although varying with time, the average rate is commensurate with that of the global mean sea-level changes. With such capacity, we filter the sea-level retrievals to be equally

https://doi.org/10.5194/egusphere-2025-3563
Preprint. Discussion started: 16 September 2025
© Author(s) 2025. CC BY 4.0 License.

sampled as a conventual tide gauge using a Kalman filter, and conduct experimental tests to investigate whether it can capture sea-level disturbances from extreme events i.e., tsunamis. Our results show that as long as the disturbances are twice larger than the standard deviation of the filtered time series, then such disturbances are successfully detected. This criterion could be largely reduced if the GNSS site was built particularly for GNSS-IR. In any case, the GNSS-IR detectability is particularly helpful to capture sea-level disturbances triggered by quiet submarine landslides as they often don't send sensible signals as earthquakes do. Our station adds an extra connecting pod to fill in the existing few stations and pushes one-step forward to link the separated land, and affords another example to study regional tectonics and sea-level variations simultaneously.

Keywords: GNSS-IR, GNSS time series, Tsunami detection, South China Sea, Sea-level variation, Nansha Islands, PCOMCOT

1 Introduction

South China Sea (SCS) basin is developed under the framework of surrounding subduction systems (Figure 1) (Li et al., 2021; Sun et al., 2009, 2019). That is the Sumatran subduction zone in the west where the Indian plate subducts underneath the Sunda plate (Chlieh et al., 2008); the Java subduction zone in the south where the Australian plate subducts beneath the Sunda plate (Koulali et al., 2018); and the Philippine subduction zone in the east where the Philippine Sea plate subducts underneath the Sunda plate (Wang and Bilek, 2014), developing a so-called super-subduction tectonic system around SCS (Li et al., 2021). Because of the interacting between SCS basin and such periphery complex subducting settings over the long-term dynamic evolution process, many tectonic elements have been grown inside the basin. These include, for instance, the Littoral Fault Zone (LFZ) in the north, which is the longest (>1000 km) fault system offshore running in parallel with the southern coastline of China (Li et al., 2022; Xia et al., 2020); and the thousand-km long Manila subduction zone (MSZ) to the northeast, and it has a comparable length to the northernmost segment of the Sumatran subduction zone where it generated the largest tsunami impact in this century (Lay, 2015); and then, the submarine landsides along both the continental slope area and Zeng Mu An Sha (ZMAS) region in the south (Gee et al., 2007; Li et al., 2019; Sun et al., 2018; Wang et al., 2018); and also volcanic process in the west and east (Paris et al., 2014; Paris and Ulvrova, 2019; Zorn et al., 2022); and finally, the reactivation major strike-

https://doi.org/10.5194/egusphere-2025-3563
Preprint. Discussion started: 16 September 2025
© Author(s) 2025. CC BY 4.0 License.

slip fault extension of the Red-River fault along the West Baram Line in the Dangerous Grounds block (e.g., Figure 1 in Clift et al., 2008). Majority of these elements are active as manifested by either historical or paleo-seismic records. For example, the eastern and western portion of the LFZ ruptured by M 7+ large earthquakes in Quanzhou 1604, Nanao 1918 & 1700, and Qiongzhou 1604, respectively (Li et al., 2022; Xia et al., 2020). Except the 1700 event, rest of the others all triggered tsunamis as evidenced in historical records, respectively (Lau et al., 2010; Li et al., 2022; Terry et al., 2017). Additionally, seafloor geomorphology and seismic surveyed data indicate that large volume of landslide body had repeatedly failed previously at both the continental slope and ZMAS regions (Gee et al., 2007; Li et al., 2019; Sun et al., 2018; Wang et al., 2018). Geologically, paleo-geological tsunami evidences are identified at various widely-distributed places in the SCS; and their dated age all point to a similar time window somewhat ~1000 years ago (Ramos et al., 2017; Yang et al., 2018; Yu et al., 2009), indicating a great tsunami event might have swept the entire basin previously, and the likely source could come from a great earthquake initiated in the MSZ (Hsu et al., 2012, 2016; Megawati et al., 2009; Qiu et al., 2019); and such a great earthquake is on the way and could repeat previous process but bring significant impact to the modern coastal megacities (Hsu et al., 2012, 2016; Li et al., 2022; Qiu et al., 2019). In such a tectonically active and high potential of facing multi-tsunami sources region in the SCS (Li et al., 2021, 2022), unfortunately, these tectonically associated processes remain poorly known, due mainly to very rare geodetic, geophysical and sea-level stations deployed in such a ~1900-km-long distance (~23°N – 6°N) between the southern coast of China and northern coast of Borneo, Malaysia (Figure 1). Particularly, in our study area - Dangerous Grounds block, it was significantly deformed with numerous shallow faults being formed during the drifting and collision process associated with the seafloor spreading development in the SCS (Das et al., 2024; Ding et al., 2013; Li et al., 2014), however, characteristics of the modern deformation and fault activities remains elusive. Essentially, our knowledge in regarding tectonics and sea-level variability in this vastly gapped area is significantly deficient; while installation of any monitoring equipment in the gapped area is quite challenging.

https://doi.org/10.5194/egusphere-2025-3563
Preprint. Discussion started: 16 September 2025
© Author(s) 2025. CC BY 4.0 License.

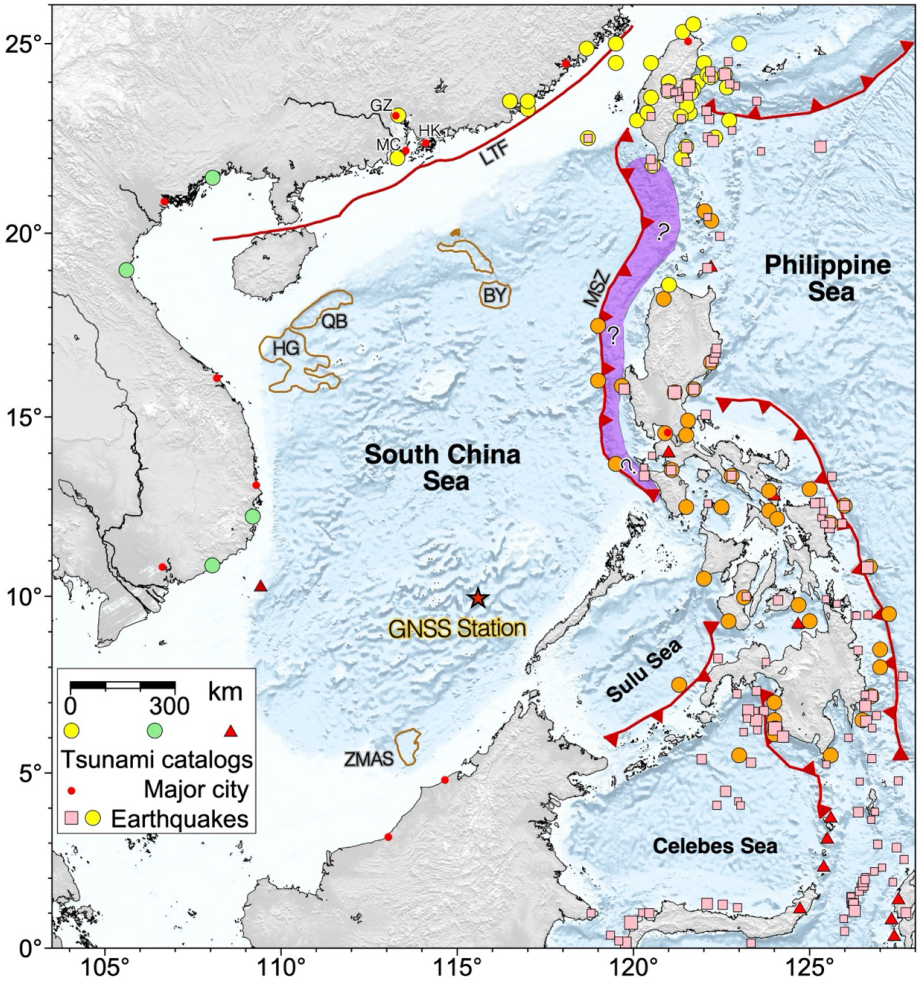

Figure 1. *Tectonic background and geographical location of the GNSS station. Red star represents the location of our coastal GNSS station in southern South China Sea. Yellow circles (Lau et al., 2010), orange circles (1589-2012, Bautista et al., 2012), green circles (Ca and Xuyen, 2008), red triangles (Paris et al., 2014) are tsunami catalogs (Li et al., 2024). LTF: Littoral fault; HG: Hua Guang submarine landslide (Wang et al., 2018); QB: Qiongdongnan submarine landslide (Wang et al., 2018); BY: Baiyun submarine landslide (Li et al., 2019; Sun et al., 2018); MSZ: Manila subduction zone; ZMAS: Zeng Mu An Sha submarine landslide (Gee et al., 2007); barbed lines: subduction zones. Pink squares: earthquake with Mw >6.5 from ANSS catalog.*

In this study, we present a recently deployed coastal GNSS station in Nansha in the Dangerous Grounds block in southern SCS (Figure 1, red star). This station locates closely to sea water area which allows us to measure sea-level variation by using GNSS-IR technique (Larson et al., 2013; Peng et al., 2021). Our results show that this single station can multi-function as both displacement

https://doi.org/10.5194/egusphere-2025-3563
Preprint. Discussion started: 16 September 2025
© Author(s) 2025. CC BY 4.0 License.

meter and sea-level measurement meter that are capable of assisting us to gain an improved understanding about the regional tectonics, and to detect extreme sea-level abnormalities, and to monitor long-term sea-level changes. We organize the content as follows. We, firstly, present the information about the GNSS station and processing procedure of its measured displacements time series; then, we briefly sum up the GNSS-IR sea-level retrieval technique; and followed by the results of GNSS displacements time series, GNSS-IR short-term sea-level measurements and its detecting capability on synthetic tsunami events, respectively; and we, then, present the long-term sea-level changes measurements; and finally, we conclude that our station is useful to study the regional tectonics and to detect both short-term sea-level extremes and long-term sea-level variations simultaneously.

2 Methodology

2.1 GNSS site and displacement measurements

Our GNSS station is deployed in June 2022 which locates at the coast facing sea water area (Figure 2b). The receiver of the GNSS is Trimble Alloy 6.16, with a 15-second sampling rate. We use GAMIT/GLOBK v10.7 program to process the GNSS data to obtain daily displacement time series (Herring et al., 2016). To achieve an accurate and stable solution, we include the nearest 14 IGS GNSS stations (e.g., anmg, bako, brun, coco, cusv, darw, dgar, hyde, iisc, jog2, ntus, pimo, pohn, and xmis) together with our GNSS in the processing procedure. Additionally, we also consider ionospheric corrections by utilizing ionospheric delay models from CDDIS during data processing (Noll, 2010). Finally, FES2014 ocean loading model (Lyard et al., 2021; Scherneck, 1991) and the Vienna Mapping Function (VMF1) model of atmospheric tropospheric delays (Boehm et al. 2006) are simultaneously included in our process for obtaining the final displacement time series. This solution allows us to monitor how the land changes in the global ITRF frame. We rotate and translate the displacement time series from ITRF to local Sunda plate frame to obtain the localized surface deformation (Altamimi et al., 2016). Details about GNSS process can be found in Herring et al. (2016). Our final displacements time series are shown in Figure 3.

https://doi.org/10.5194/egusphere-2025-3563
Preprint. Discussion started: 16 September 2025
© Author(s) 2025. CC BY 4.0 License.

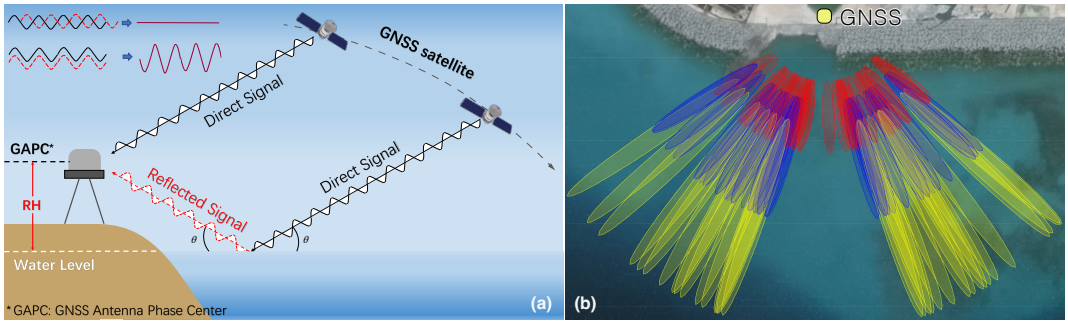

Figure 2. *Conceptual map for geometry of the GNSS-IR and example of reflection zones at our coastal geodetic GNSS station. (a) geometry of a coastal geodetic GNSS station for GNSS-IR; (b) reflection zone at our coastal geodetic GNSS station with colors marking elevation angles (red:5, blue:7, yellow:10).*

2.2 GNSS-IR for sea-level retrievals

A space satellite sends signals that can be directly received or reflected by the ground objects and then received by a ground-based geodetic receiver. The reflected signals are often removed as they cause multi-path effects when analyzing the geodetic displacements. However, they can be quite useful to retrieve sea-level variations if the GNSS station is deployed closely enough to sea area. Indeed, Larson et al. (2013) and Roesler and Larson (2018) have demonstrated that a single geodetic GNSS receiver actually records the signals from the interference between direct signals and reflected signals. These interference signals can be expressed in the SNR data of GNSS observational files (Larson et al., 2013). Under this framework, they have developed the GNSS-IR (GNSS-Interferometric Reflectometry) technique to retrieve sea-level variations based on the geometry of coastal geodetic GNSS station (Roesler and Larson, 2018) (Figure 2a). We briefly sum up the key points in this section.

The geometric relationship of the principle of GNSS-IR is shown in Figure 2a. From the simple geometry relationship, the path difference D between the direct signal and the reflected signal can be obtained from the geometric relationship.

$$D = 2Hsine \qquad (2-1)$$

The wavelength of the satellite signal is λ, and the phase difference φ between the direct signal and the reflected signal are obtained:

$$\varphi = \frac{4\pi H}{\lambda} sine \qquad (2-2)$$

https://doi.org/10.5194/egusphere-2025-3563
Preprint. Discussion started: 16 September 2025
© Author(s) 2025. CC BY 4.0 License.

From (2-2), if sine is treated as a variable, then:

$$2\pi f = \frac{d\varphi}{dsine} = 4\pi \frac{H}{\lambda} \quad (2-3)$$

Where f is the frequency of SNR characteristic oscillation that overlays a long-term trend, and thus, the relationship between f and H can be further obtained as

$$f = \frac{2H}{\lambda} \quad (2-4)$$

Thus, the SNR data is mainly a long-period variation caused by the distance of the receiver from the satellite and the gain pattern of the antenna (Figure 2). Following Larson et al. (2013), we firstly converted the SNR data from logarithmic scale decibel-hertz to a linear scale volts/volts format, and then conducted a low-order polynomial fits to remove the trend for residual SNR signals, and then, with the residual signals, we further performed a Lomb-Scargle Periodogram (LSP) analysis to obtain the characteristic frequency term f, and finally, we calculated the reflection height H to retrieve the relative sea-level variation. In these calculations, the sea surface is assumed to be stationary when satellite signal can be received during the ascending and descending processes. However, in reality, the sea surface is constantly changing and sometimes can be violent, therefore, a Reflection Height-Rate Correction (RHRC) is required. We performed the RHRC correction following the algorithms of Larson et al. (2013). Additionally, the tropospheric delay could also affect the final estimates on H (Peng et al., 2019), therefore, we further corrected the delayed effect by a combination of astronomical refraction (G. G. Bennett, 1982), GPT2 (Global Pressure and Temperature 2), and Wet model (Böhm et al., 2015). Details on GNSS-IR, RHRC and tropospheric delay corrections can be found in series of previous studies (Larson et al., 2013; Roesler and Larson, 2018).

2.3 Tsunami detection using synthetic tsunami sources

The GNSS-IR retrieved sea-level measurements are often unequally sampled in time. Such sampling rate highly depends on the reflection environment of a particular site (Figure 2). Ideally,

https://doi.org/10.5194/egusphere-2025-3563
Preprint. Discussion started: 16 September 2025
© Author(s) 2025. CC BY 4.0 License.

if the range of the azimuthal angle and elevation are sufficient wide, then a denser sampling rate is achieved (Figure 2b). Further, through combing multiple frequencies and satellite constellations (Larson et al., 2021; Li et al., 2024; Tu et al., 2021), the rate can be significantly improved e.g., in some cases, the average sampling rate can reach ~6 mins that is comparable to a conventional tide gauge measurement (Li et al., 2024). Integrating such high sampling rate and a Kalman filter technique, one can filter the GNSS-IR sea-level measurements to a same sampling rate with tide gauge to detecting short wavelength sea-level events e.g., tsunamis (Larson et al., 2021; Li et al., 2024), and even to do real time sea-level monitoring (Strandberg et al., 2019). Following our previous work (Li et al., 2024), we integrate the sea-level retrievals measured by multi-frequencies and multi-satellite constellations of our GNSS station and Kalman filter to derive an equally-sampled interval sea-level time series to compare with that from a co-located tide gauge. We then use this filtered sea-level time series to perform experimental tests on tsunami detections using synthetic tsunamis events.

Global review studies indicate that a typically Mw 8.4 or higher subduction earthquake could generate tsunami run up larger than 3 meters that can cause potential damage and hazard in the coastal area (Cheung et al., 2022; Qiu and Barbot, 2022). Comparatively, a shallow tsunami earthquake with one order of magnitude smaller can also generate significant tsunami hazards (Hill et al., 2012; Kanamori, 1972; Polet and Kanamori, 2000; Qiu and Barbot, 2022). In SCS, the MSZ is the most likely candidate that can initiate subduction zone earthquakes with Mw >8+ (Hsu et al., 2012, 2016; Zhao and Niu, 2024). Tsunami earthquake in the MSZ is possible but less likely, since none such events were never ever recorded or reported previously (Lau et al., 2010; Terry et al., 2017). In this case, we consider a typical synthetic Mw 8.4 earthquake that is one representative model retrieved from the sample model database used in previous probabilistic tsunami hazard assessment (PTHA) study in the SCS (Li et al., 2016, 2018). This sample model has majority of the slip at the seismogenic depth (case 1) which does not take into account the shallow large slip effect that is likely responsible for the exaggerated tsunami hazard being observed in the 2011 Mw 9.1 Tohoku-Oki event (Lay, 2018; Lay and Kanamori, 2011). Therefore, we select another representative sample model from the database to mimic such shallow tsunami excitation effect (case 2). These two representative models all located in the southern segment of the MSZ (Figure S1), where the triggered tsunamis propagate directly towards our GNSS station, allowing a maximum detecting efficiency on the incoming tsunami waves (Figure 1). To maximumly and

https://doi.org/10.5194/egusphere-2025-3563
Preprint. Discussion started: 16 September 2025
© Author(s) 2025. CC BY 4.0 License.

completely take into account the potential multiple tsunami sources, we also consider a representative synthetic landslide tsunami scenario (case 3) triggered by the ZMAS submarine landslide in southern SCS (Li et al., 2019, 2022) (Figure 1).

Our synthetic tsunami scenarios contain sources from both the subduction zone earthquakes and submarine landslides. For subduction zone earthquakes, the typical wavelength of tsunami is hundreds of km and thus, is sufficiently large enough compared to local a-few km deep water depth, therefore, dispersive effect is not necessarily considered in wave propagation modeling; in contrast, submarine landslide triggered tsunamis often occur in deep water, and the wavelength of the tsunami is not significantly large as compared to local water depth. In this case, the wave dispersive effect is significant and is needed to be modeled during wave propagation. We use PCOMCOT software to model these synthetic tsunami events. The software is an updated code from COMCOT (**Co**rnell **M**ulti-grid **Co**upled **T**sunami) model (Wang and Liu, 2006, 2007), which is paralleled with MPI, more recently with GPU and can efficiently simulate dispersive, breaking and nonlinear wave phenomenon within the framework of shallow water equations (Zhu et al., 2024). For the bathymetry data, we use the best available GEBCO24 bathymetry and topography for modeling the tsunami wave propagation in the SCS. We model a 5-hour physical time of tsunami wave propagations in the SCS.

3 Results

3.1 Land displacements changes monitored by GNSS

Figure 3 shows the nearly a-year displacement time series recorded at our GNSS station. In general, displacements of all the three components over this monitoring period is small, with the horizontal components ~4-5 mm and the vertical component ~1 cm, respectively (Figure 3a, b and c). The overall trend for all the three components is generally flat, with a least-squares estimated average rate of 7.8 ± 0.95mm/yr, 2.8 ± 0.66 mm/yr and 1.1 ± 3.13 mm/yr in the east, north and vertical component, respectively. To extract the general motion of the GNSS site as evidenced by the displacements while considering the measurement noise, we performed a Kalman filter analysis (Li et al., 2024). Our results show that a consistent displacements changes do occur at each of the three components between year 2024.25 to 2024.35 (Figure 3a, b and c). In this particular time window, the displacements reach the largest in both horizontal and vertical components. Such outstanding displacements changes are successfully captured in all the three components, and thus, are likely real signals. If so, these changes might have associated with a localized time-varying

https://doi.org/10.5194/egusphere-2025-3563
Preprint. Discussion started: 16 September 2025
© Author(s) 2025. CC BY 4.0 License.

geological process. In summary, the land here is generally stable, occasionally with a few to tens of mm displacement changes, possibly as a result of localized geological process.

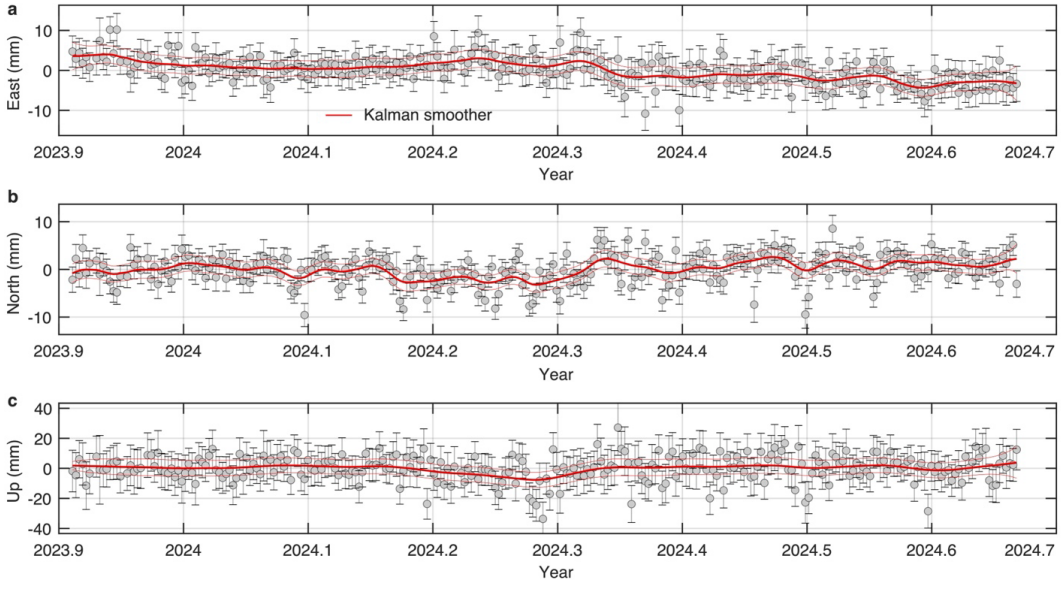

Figure 3. *Yearly-long displacements time series at our GNSS station. (a), (b) and (c) show the daily displacements time series for the east, north and up component, respectively. Heavy and thin red curves are the smoothed Kalman-filter fits and their corresponding 2-standard deviation estimates.*

3.2 GNSS-IR sea-level retrievals and its validation

We, firstly, present a short-term time period GNSS-IR sea-level retrievals and its validation in Figure 4. And we, then, present a long-term sea-level retrievals validation in Figure 5. Figure 4 shows our sea-level retrievals covering three periods in July and August 2023, respectively. These results indicate that the average sampling rate can be quite variable at different time within a year. In these periods, the maximum sampling rate reaches ~50 per day (~30 mins), and the lowest rate reaches ~20 per day (~1h). In particular, middle and late of August 2023 have ~20–40 rates per day (~40 mins to 1 h); while early July 2023 general has higher rates between ~30–50 per day (~28 to 48 mins) except the lower rate at the first day (~1h). Intriguingly, we notice a general phenomenon. That is when sampling rates are lower and sea-level oscillations are stronger, then the sea-level retrievals are relatively noisier (Figures 4 and 5). In any cases, despite the reflection environment is not an ideal case (Figure 2b), the sea-level retrievals still capture the nature of time-varying characteristics remarkably well, and are commensurate with the recordings from the nearby tide gauge (Figures 4 and 5).

https://doi.org/10.5194/egusphere-2025-3563
Preprint. Discussion started: 16 September 2025
© Author(s) 2025. CC BY 4.0 License.

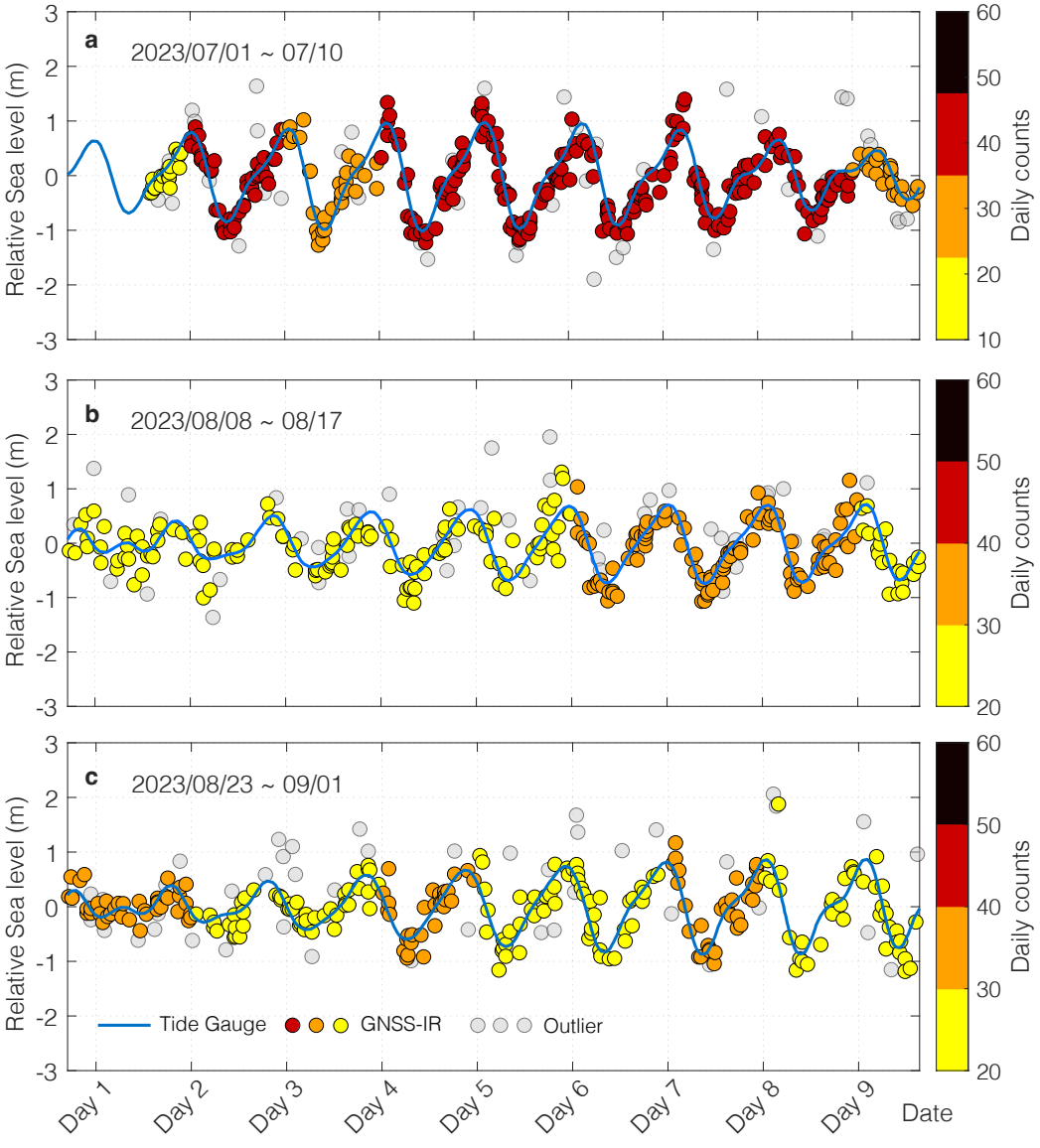

Figure. 4. *An example of multiple short-term GNSS-IR sea-level retrievals validations with tide gauge. (a), (b) and (c) GNSS-IR sea-level retrievals validation with tide gauge measurements over 01 July 2023 to 10 July 2023, 08 August 2023 to 17 August 2023, and 23 August 2023 to 01 September 2023 time windows, respectively. Colors on circles show daily average measurement counts.*

https://doi.org/10.5194/egusphere-2025-3563
Preprint. Discussion started: 16 September 2025
© Author(s) 2025. CC BY 4.0 License.

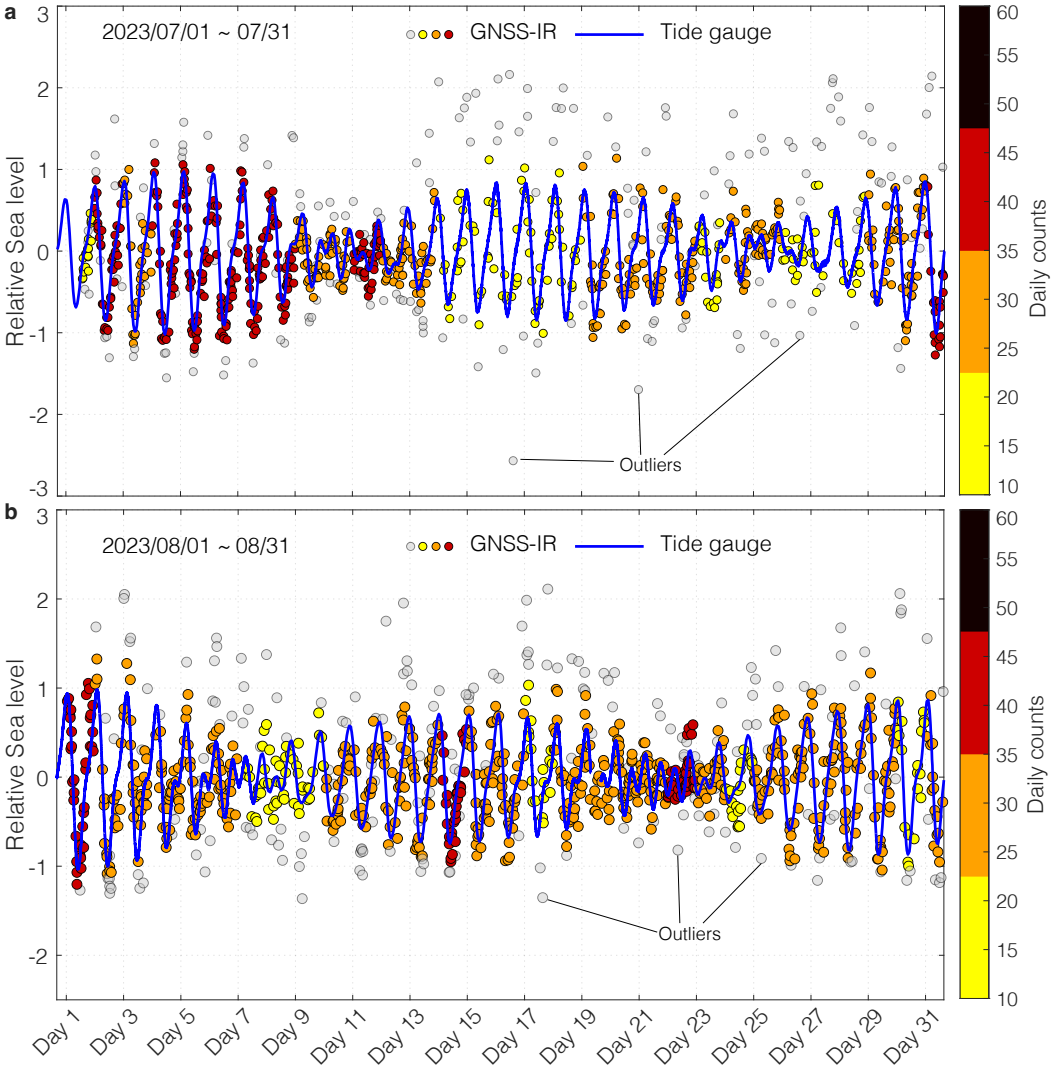

Figure 5. *An example of multiple monthly GNSS-IR sea-level retrievals validations with tide gauge measurements. (a) validation for July 2023; (b) validation for August 2023. Colors on circles show daily average measurement counts.*

We further extend the validation to monthly long-term time periods (Figure 5). Our results demonstrate that the sea-level retrievals reveal a same phenomenon as obtained from the short-term time periods validation. That is when the average daily sampling rate is lower than 20, then the retrievals are relatively more scattering as manifested e.g., day 13 to 19 in July 2023, and day 2 to 9, 17 and 24 in August 2023; while when the sampling rate is higher that 20, then the

https://doi.org/10.5194/egusphere-2025-3563
Preprint. Discussion started: 16 September 2025
© Author(s) 2025. CC BY 4.0 License.

measurements are lesser scattering as shown in both July and August 2023. Despite the sea-level retrieval time series is, sometimes, scattering, with outliers removed, the amplitude variations from day by day and the trend are well captured by the GNSS-IR measurements, which compare remarkably well with the tide gauge recordings (Figures 4 and 5). From above both the short-term and long-term time periods sea-level retrievals validations, we conclude that our coastal GNSS station is capable of monitoring the sea-level variations. This conclusion helps us to build confidence on using the station to detect sea-level extreme events e.g., storm surges (Li et al., 2024; Peng et al., 2019), tsunamis (Larson et al., 2021) and sea-level changing phenomenon (Larson et al., 2013; Peng et al., 2021) in the SCS.

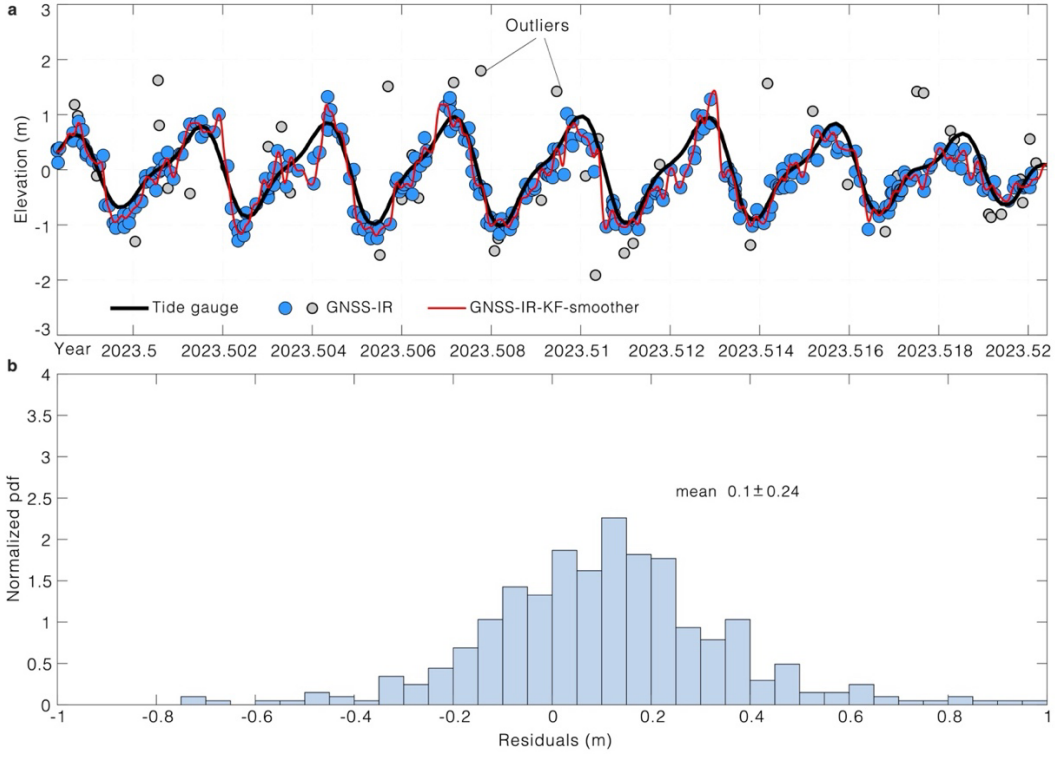

Figure 6. *An example of quantitative comparison between Kalman-filtered GNSS-IR sea-level retrievals and tide gauge. (a) Comparison between Kalman-filtered GNSS-IR sea-level retrievals (circles) and tide gauge recordings (black curve) over 01 July 2023 to 10 July 2023 time window. Red curve is the Kalman-filtered sea-level time series from the GNSS-IR sea-level retrievals (blue circles); (b) histograms of residuals between Kalman-filtered GNSS-IR sea-level retrievals and tide gauge recordings.*

https://doi.org/10.5194/egusphere-2025-3563
Preprint. Discussion started: 16 September 2025
© Author(s) 2025. CC BY 4.0 License.

To quantify the exact difference between the GNSS-IR and tide gauge measurements, we, firstly, use a Kalman filter to process the original uneven sampled GNSS-IR sea-level retrievals to be the same minute-sampling rate with the nearby tide gauge (Li et al., 2024); we then subtract the tide gauge recordings by the filtered sea-level time series; and finally, we calculate the mean and standard deviation from the residuals. We show one example between July 1 to 10 of 2023 in Figure 6, and the others (either short- or long-term) follow a similar statistics feature. Overall, the residuals reach a mean that is close to zero with a standard deviation about 20% of the maximum amplitude (Figure 6). Our further experimental tests indicate that a smoother filtering process will slightly reduce the standard deviation by a few cm, but it will be inefficiently to detect sea-level abnormalities that will be smeared out by a smoother filtering. We will discuss this effect in the discussion section.

3.3 GNSS-IR detection on tsunami waves

The modeled maximum tsunami wave amplitudes for the seismogenic (case 1) and shallow slip (case 2) subduction earthquake scenario are shown in Figure 7a and b, respectively. We obtain relatively a lesser tsunami impact for the seismogenic earthquake case with amplitudes higher than 3 meters in the rupture zone, and smaller than a meter at other places (Figure 7a and d); in contrast, the shallow slip earthquake scenario causes significant tsunamis in and out of the rupture zone with amplitudes reaching 2–3 m at both our study area and western coast of Palawan, less than 1 m in the far field (Figure 7 b and d). In the near-field, the tsunami amplitudes are comparable for these two cases (Figure 7 a and b). For the ZMAS submarine landslide scenario (case 3), if the model simply reproduces one of the repeated historical cases (Gee et al., 2007; Li et al., 2022), then the triggered tsunamis cause significant impact in southwestern SCS (Figure 7c and d) (Li et al., 2019). That is the northwest coast of Borneo receives the highest impact where the wave amplitudes are >5 m; then followed by southwestern SCS including our study area where the wave amplitudes are 4–8 m (Figure 7c and d); and then the southeast coast of Vietnam where the amplitudes are 4–5 m or even >5 m at some places; and finally, the western coast of Palawan where the wave amplitudes range 2–4 m (Figure 7c).

The synthetic tsunami waveforms at our study area are shown in Figure 7d. To demonstrate whether the GNSS-IR sea-level retrievals at our GNSS coastal geodetic station can detect such water level abnormalities or not. We, firstly, overlay these waveforms to the original GNSS-IR sea-level retrievals e.g., where it has higher sampling rate (red line in Figure 8); and then filter the sea-level retrievals using a Kalman filter and finally, with such superimposed signals, we perform a wavelet analysis to detect any frequency modulations caused by tsunami waves if there were some. Our experimental detecting results for seismogenic, shallow subduction earthquake and

https://doi.org/10.5194/egusphere-2025-3563
Preprint. Discussion started: 16 September 2025
© Author(s) 2025. CC BY 4.0 License.

submarine landslide scenario is shown in Figures 8a, b and c, respectively.

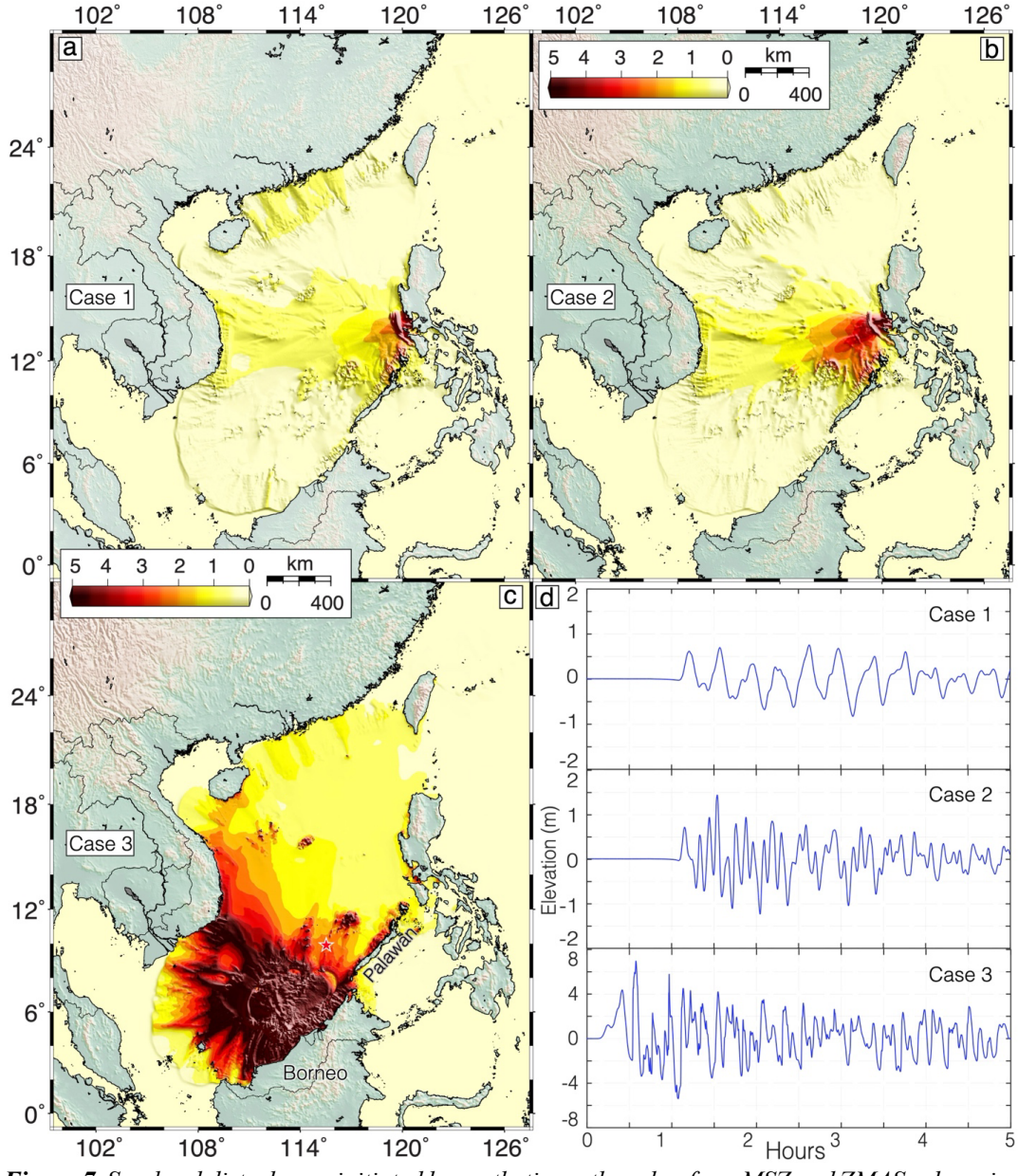

Figure 7. *Sea-level disturbance initiated by synthetic earthquakes from MSZ and ZMAS submarine landslide scenarios. (a) and (b) maximum wave amplitudes modeled with a typical Mw 8.4 seismogenic and a shallow subduction earthquake, respectively. (c) maximum wave amplitudes modeled with the ZMAS submarine landslide with red star marking the location of the wave gauge.*

https://doi.org/10.5194/egusphere-2025-3563
Preprint. Discussion started: 16 September 2025
© Author(s) 2025. CC BY 4.0 License.

(d) the corresponding recorded synthetic tsunami waveforms at wave gage show in (c) (also shown in Figure 1).

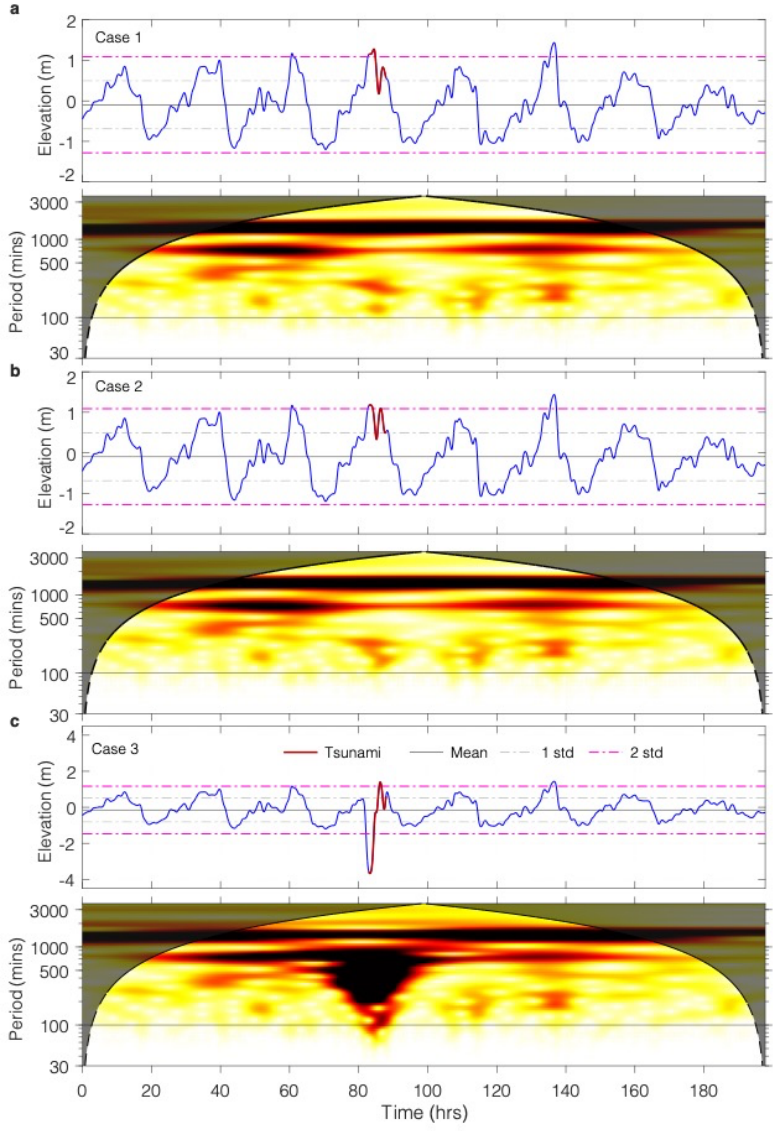

Figure 8. *Experimental tests on sea-level abnormalities detecting using the Kalman-filtered GNSS-IR sea-level retrievals. (a), (b) and (c) the time and frequency analysis for synthetic scenarios about a typical Mw 8.4 seismogenic (Figure 7a), a shallow Mw 8.4 subduction zone earthquake in MSZ (Figure 7b) and the ZMAS submarine landslide (Figure 7c), respectively.*

For tsunami waveforms overlaid within higher sampling rate (>30 average daily counts) at different time windows, the detecting effect is similar (Figure S2). We note that for all scenarios,

https://doi.org/10.5194/egusphere-2025-3563
Preprint. Discussion started: 16 September 2025
© Author(s) 2025. CC BY 4.0 License.

the frequency abnormalities are fairly well captured by the GNSS-IR technique, suggesting the Kalman filter-based GNSS-IR retrievals is an efficient way to detect tsunamis. The detected wave periods for the two subduction earthquakes are ~100 mins which is more than twice larger than the original wave periods but are sufficiently smaller than the background frequencies (e.g., >300 mins) (Figures 8 and S3-S4); and for the submarine landslide, it is ~40 mins which is comparable with the original time period (Figure S5). Overall, our GNSS-IR, although not ideally for reconstructing the natural frequency of the synthetic tsunami waves, it still can detect such wave disturbances or abnormality caused by these marine geological processes (Larson et al., 2021; Li et al., 2024; Peng et al., 2019).

4 Discussions

Our geodetic time series indicate the nearly one-year 3D displacements vary within ~4–5 mm in horizontal components and ~1 cm in vertical (Figure 3). In addition, the displacements for each component are nearly flat except a compelling transient change in between year 2024.2.7 and 2024.3.7 with a maximum amplitude reaching ~9–10 mm. This transient process generates a cumulative displacement ~4 mm in the north, ~5 mm in the east and ~9–10 mm in the up component, respectively (Figure 3). These displacements and trend variations are significantly larger than the measurement errors that are often ~1–2 mm in the horizontal and ~3–7 mm in the vertical (Feng et al., 2015a, b), they are ~3 mm in the horizontal and ~10 mm in the vertical estimated in our data processing, respectively. Additionally, all the three components captured these distinctive displacements changes by the Kalman filter, we conclude that the transient process is likely real, and will continue validating it through examining the high-sensitive strain measurements recorded by a co-located strain meter in our following study. By integrating the displacements and strain measurements, then hopefully, we can narrow down to find out the potential geological process. Except for the trainset process, the displacements don't show much linear trend as typically seen at other tectonically active regions where the tectonic plates are continuously moving (Chlieh et al., 2008; Loveless and Meade, 2016), but instead, show, in general, a flat trend (Figure 3). A flat trend suggests that the monitored area is quite stable. Indeed, our GNSS site locates on the right flank of middle ridge on the Dangerous Grounds block in the southwestern SCS basin, where a major strike-slip fault is reactivated to the west boundary of the block (Figure 1 in Clift et al., 2008). Additionally, the SCS basin starts to open and grow ~33 Ma

https://doi.org/10.5194/egusphere-2025-3563
Preprint. Discussion started: 16 September 2025
© Author(s) 2025. CC BY 4.0 License.

ago (Li et al., 2014) under the effect of the surrounding large-scale geological processes i.e., collision between the Indian and Eurasian plate to the northwest (Tapponnier et al., 2001) and, the super-subduction system from west, south to east (Li et al., 2021). Then, the basin seems to stop growing at ~15–16 Ma, with a life span ~17–18 Ma (Li et al., 2014). A dead basin maintains a tectonically stable environment within Sunda land, and thus seismically quiet, as manifested by the seismicity observation since 1900 (Figure 1 and S6), and by the nowadays flat displacements measured at our GNSS (Figure 3). Whether the strike-slip fault along the West Baram Line in the Dangerous Grounds block is active or not cannot be determined by our single station, future more stations, at least several, deployed on both sides of the fault can help address this question. Our unique GNSS site will continue monitoring such quiet environment and pick abnormal geological process if there were some in the following years; and also works as foundation to step forward on bridging the mainland China and northern Borneo of Malaysia and eventually filling our knowledge gaps in this wide area.

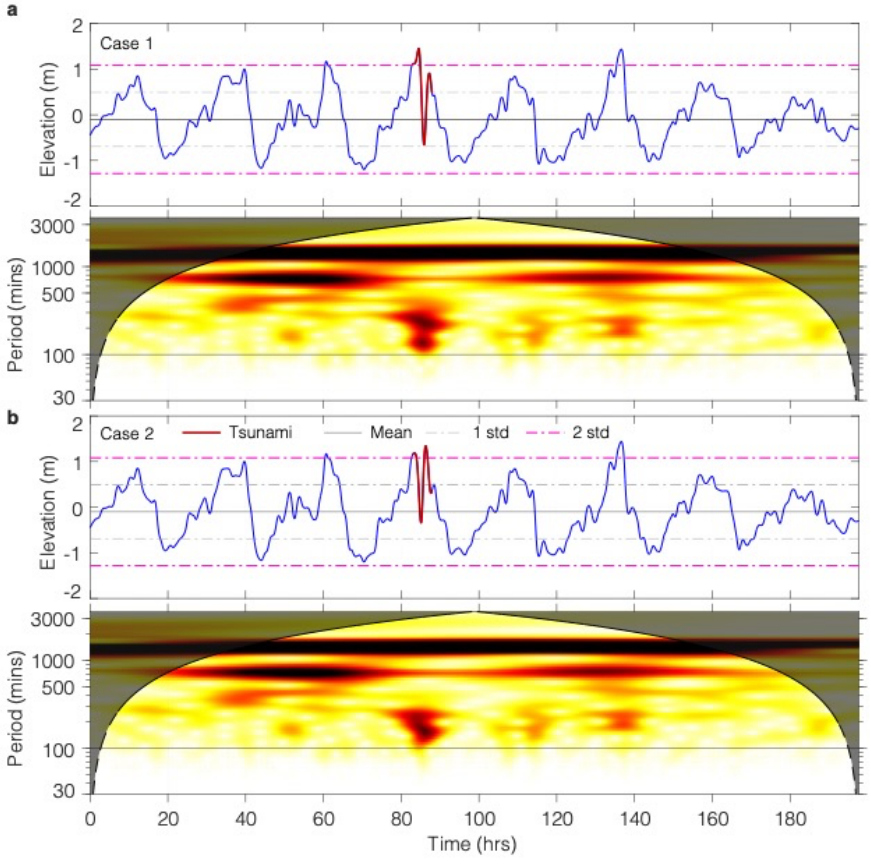

https://doi.org/10.5194/egusphere-2025-3563
Preprint. Discussion started: 16 September 2025
© Author(s) 2025. CC BY 4.0 License.

Figure 9. *Experimental tests on detecting sea-level abnormality caused by a general seismogenic (a) (case 1 by scaling the waveform) and shallow subduction zone earthquake (b) (case 2 by scaling the waveform).*

The GNSS-IR sea-level retrievals show that the maximum average daily sampling rate is ~50, equivalent to ~ 30 mins per measurement that is comparable to the wave period generated by a typical subduction zone earthquake (Figures 6 and S3–S4). Basically, we have one measurement point per cycle of tsunami wave, which is way too sparse to capture any details of tsunami waveforms. Our previous study demonstrates that the average sampling rate should at least higher than 6–16 mins, and then its Kalman-filtered sea-level retrievals could be comparable with a co-located tide gauge measurements within a few cm uncertainty (Figure 4, in Li et al., 2024). Essentially, our coastal GNSS is not an ideal case to capture full tsunami waveforms to be used for reconstructing an earthquake source from e.g., the MSZ and eventually for early warning (Li et al., 2024); and also, a further smoothed filtering process will smear out the abnormalities, resulting in undifferentiable frequency in the wavelet analysis. However, our GNSS station still can detect sea-level abnormalities if we don't aim to reconstruct the natural frequencies of such disturbance. In this content, as long as these abnormalities are higher than the sea-level background variation by twice larger the standard deviation of the filtered entire time series (Figures 8 and 9). This is crucial because some marine geological processes occur without sending out detectable signals as earthquakes do, for instance, the submarine landslide. In this case, our GNSS-IR would be very useful to detect such quiet tsunami waves when they came (Figure 8c). This is particular important in SCS in several aspects. Because a handful of large submarine landslides have been identified in both northern and southern SCS (Figure 1, Sun et al., 2018; Wang et al., 2018). Many more could be identified along the continental slop from south of Hainan to southwest of Taiwan following extensive marine geological surveys in future (Figure 1). For those identified slides, their volumes are measured and their tsunami impacts are assessed (Li et al., 2019, 2022; Pan et al., 2022). If these, for example, the ZMAS slide repeated one of the previous case again, the triggered tsunami waves will be detected as sea-level abnormalities from our GNSS-IR technique (Figure 8c); and if several (e.g., 2 to 3) similar GNSS stations were deployed at other places with difference orientations in the Nasha region, then we can figure out where the possible source comes from based on the time differences measured at these sites and wave travelling speed, and also differentiate the type of sources from the frequency differences (Figures 8, 9 and S2–S4). Once we

https://doi.org/10.5194/egusphere-2025-3563
Preprint. Discussion started: 16 September 2025
© Author(s) 2025. CC BY 4.0 License.

assure the possible location and type of the source, a rapid tsunami information can be retrieved from a precomputed database and sent out for evacuation and warning process (Xu et al., 2021); and thus, the confirmed products can be sent out in time and are extremely important for the middle and far-field regions e.g., central-eastern Vietnam, western Luzon and southern Hainan, China, potentially saving more lives, before waves' attack (Figure 7c). This process is possible as both the GNSS and GNSS-IR process nowadays can be made in real time (Chen et al., 2020; Kawamoto et al., 2016; Strandberg et al., 2019). In some cases, the existing tide gauge could be damaged but our GNSS station could be survived as it is deployed tighten by concrete structure a-few meters above the mean sea level (Li et al., 2024). Consequently, this idea could be an extra component to complement current tsunami early warning systems in the SCS and elsewhere (Mori et al., 2022).

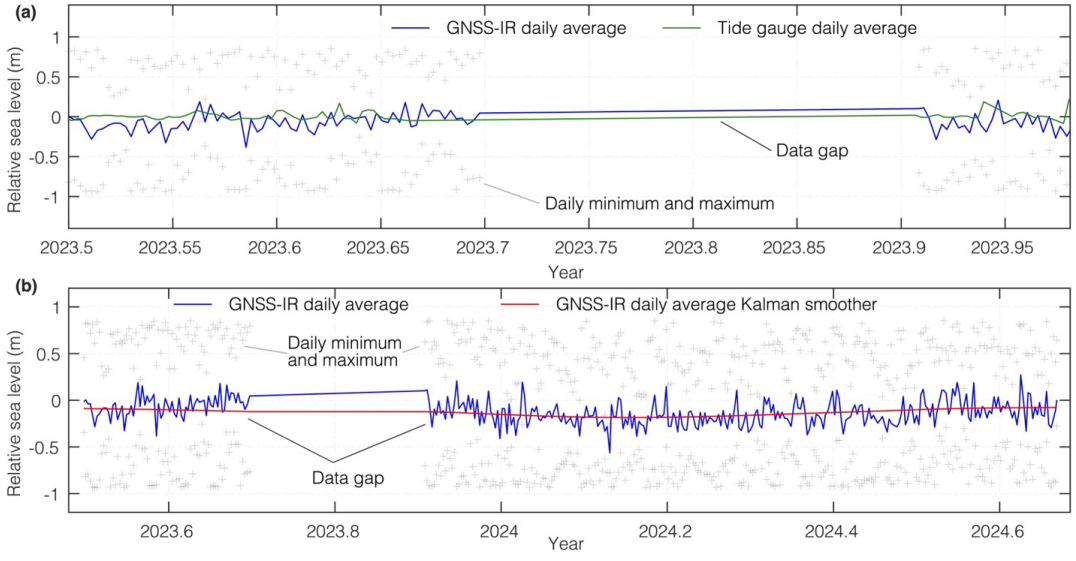

Figure 10. *Comparison between yearly-long daily-averaged sea-level retrievals from GNSS-IR and daily-averaged sea-level measurements from tide gauge. (a) the daily averaged sea-level comparison between GNSS-IR (blue) and tide gauge (green). (b) yearly-long daily-averaged GNSS-IR sea-level retrievals and its Kalman filter smoother.*

Our both weekly- and monthly GNSS-IR sea-level retrievals validation examples with tide gauge illuminate that these retrievals can capture both the amplitude variation and trend fairly well, although it is somewhat nosier and sparser (Figures 4 to 6). For long-term sea-level validation, we calculate the daily average sea-level variations for the year-long data and validate that with the limited tide gauge measurements (Figure 10a). We obtain, in general, a fairly well matching

https://doi.org/10.5194/egusphere-2025-3563
Preprint. Discussion started: 16 September 2025
© Author(s) 2025. CC BY 4.0 License.

between the GNSS-IR results and tide gauge recordings, with an average rate of 3.5 ± 0.6 cm/yr measured by tide gauge and 1.6 ± 1.8 cm/yr measured by GNSS-IR over the available data window. Although, the rate is not exactly the same, they are comparable. Overall, the long-term sea-level validation between our GNSS-IR and the tide gauge show a commeasurable magnitude; and the difference emerges due mainly to the data gaps and the limited data of tide gauge; and it is also possible due to the nosier and scattered sea-level retrievals measured by the relatively coarse sampling rate from the undesirable reflection geometry and rough sea surface (Larson et al., 2013b); but less likely due to the vertical land changes as it is generally flat in long-term time periods (Figure 2c). However, for a long-term period, in fact, the yearly daily-averaged sea-level retrievals from GNSS-IR show an estimated average rate ~3.4 ± 4.6 mm/yr (red line) that is a comparable magnitude to that estimated in both regional in SCS and global sea-level studies (Figure 10b) (Cazenave and Moreira, 2022; Chen et al., 2024; Frederikse et al., 2020; Hamlington et al., 2024; Han et al., 2021; Hay et al., 2015; Horton et al., 2018; Wang et al., 2022). We will further validate our longer GNSS-IR sea-level retrievals with tide gauge when more GNSS data come in and longer tide gauge data becoming available in following years; and our simultaneously measurements on vertical land displacements and relative sea-level variations from GNSS-IR could help us to gain a comprehensive understanding about the contributions to local and global sea-level changes (Frederikse et al., 2020; Hamlington et al., 2024).

5 Conclusions

We present a coastal GNSS station that can measure land displacements in mm precision, and retrieve sea-level variations in cm precision using the GNSS-IR technique in the southern SCS. We find that the yearly land displacements vary within a few mm in both the horizontal and vertical components, and are generally stable. The displacements time series are pretty flat without seeing a linear trend, but are occasionally disturbed by a subcentimeter change. The GNSS-IR sea-level retrievals are comparable with the tide gauge measurements in both short- and long-term observational time windows, capturing weekly, monthly and yearly amplitude variations and trend adjustments. Such ability allows us to detect sea-level abnormalities that could be generated by earthquakes and quiet submarine landslides. This station works as a linkage to further bridge southern mainland China to northern Borneo, Malaysia to gain new knowledge about the tectonics in between, and to detect sea-level disturbances generated by extreme events, and finally, to

https://doi.org/10.5194/egusphere-2025-3563
Preprint. Discussion started: 16 September 2025
© Author(s) 2025. CC BY 4.0 License.

capture long-term sea-level trend variations for a better understanding about regional and global sea levels.

Acknowledgements

This work is funded by the National Key R&D Program of China (No. 2022YFC3102200), Guangdong Province Introduced Innovative R&D Team of Big Data - Mathematical Earth Sciences and Extreme Geological Events Team (2021ZT09H399) and Innovation Group Project of Southern Marine Science and Engineering Guangdong Laboratory (Zhuhai) (No. 311023002). We are grateful to all the researchers, engineers from Nansha Center and South China Sea Institute who have helped with the logistic, support and installation of the GNSS station. Figures are generated by using GMT software (Wessel et al., 2013, 2019) and Matlab.

Data statement

The seismicity analysis in this study can be retrieved from the USGS, ANSS catalogs through the link https://earthquake.usgs.gov/earthquakes/search/; https://earthquake.usgs.gov/data/comcat/, respectively. The slip models (case 1, case 2 and case 3) are retrieved from previous studies (Li et al., 2016, 2018, 2022) and could be obtained upon reasonably request. Tsunami modelling code can be obtained through the link https://github.com/yifanzhu-fluid/PCOMCOT.

References

Altamimi, Z., Rebischung, P., Métivier, L., and Collilieux, X.: ITRF2014: A new release of the International Terrestrial Reference Frame modeling nonlinear station motions, J Geophys Res Solid Earth, 121, 6109–6131, https://doi.org/10.1002/2016JB013098, 2016.

Bautista, M. L. P., Bartolome C. Bautista, Salcedo, J. C., and Narag, I. c.: Philippine Tsunamis and Seiches, Philippine Institute of Volcanology and Seismology, 111 pp., 2012.

Böhm, J., Möller, G., Schindelegger, M., Pain, G., and Weber, R.: Development of an improved empirical model for slant delays in the troposphere (GPT2w), GPS Solutions, 19, 433–441, https://doi.org/10.1007/s10291-014-0403-7, 2015.

Ca, V. and Xuyen, N. D.: Tsunami risk along Vietnamese coast, 2008.

Cazenave, A. and Moreira, L.: Contemporary sea-level changes from global to local scales: a review, Proceedings of the Royal Society A, 478, https://doi.org/10.1098/RSPA.2022.0049, 2022.

https://doi.org/10.5194/egusphere-2025-3563
Preprint. Discussion started: 16 September 2025
© Author(s) 2025. CC BY 4.0 License.

Chen, K., Liu, Z., and Song, Y. T.: Automated GNSS and Teleseismic Earthquake Inversion (AutoQuake Inversion) for Tsunami Early Warning: Retrospective and Real-Time Results, Pure Appl Geophys, 177, 1403–1423, https://doi.org/10.1007/S00024-019-02252-X/FIGURES/11, 2020.

Chen, M., Yan, H., Jin, Y., Wang, T., and Yang, J.: Observed Sea Level Changes in the China Seas Since the 1990s, Lecture Notes in Civil Engineering, 394 LNCE, 1023–1032, https://doi.org/10.1007/978-981-99-7409-2_93/FIGURES/7, 2024.

Cheung, K. F., Lay, T., Sun, L., and Yamazaki, Y.: Tsunami size variability with rupture depth, Nat Geosci, 15, 33–36, https://doi.org/10.1038/s41561-021-00869-z, 2022.

Chlieh, M., Avouac, J. P., Sieh, K., Natawidjaja, D. H., and Galetzka, J.: Heterogeneous coupling of the Sumatran megathrust constrained by geodetic and paleogeodetic measurements, J Geophys Res, 113, 1–31, https://doi.org/10.1029/2007JB004981, 2008.

Clift, P., Lee, G. H., Anh Duc, N., Barckhausen, U., Van Long, H., and Zhen, S.: Seismic reflection evidence for a Dangerous Grounds miniplate: No extrusion origin for the South China Sea, Tectonics, 27, https://doi.org/10.1029/2007TC002216, 2008.

Das, P. S., Choudhuri, M., Zakaria, N. L., Tengku Hassan, T. M. S. B., Rudiana, C. W., and Mohd Idris, J. J. B.: Review and new insights on the significant unconformities related to the strati-structural evolution of NW Sabah within the Dangerous Ground, South China Sea, Arabian Journal of Geosciences 2024 17:1, 17, 1–22, https://doi.org/10.1007/S12517-023-11828-W, 2024.

Ding, W., Franke, D., Li, J., and Steuer, S.: Seismic stratigraphy and tectonic structure from a composite multi-channel seismic profile across the entire Dangerous Grounds, South China Sea, Tectonophysics, 582, 162–176, https://doi.org/10.1016/J.TECTO.2012.09.026, 2013.

Feng, L., Hill, E. M., Banerjee, P., Hermawan, I., Tsang, L. L. H., Natawidjaja, D. H., Suwargadi, B. W., and Sieh, K.: A unified GPS-based earthquake catalog for the Sumatran plate boundary between 2002 and 2013, J Geophys Res Solid Earth, 120, 3566–3598, https://doi.org/10.1002/2014JB011661, 2015a.

Feng, L., Hill, E. M., El, P., Qiu, Q., Iwan, H., Banerjee, P., and Sieh, K.: Hunt for slow slip events along the Sumatran subduction zone in a decade of continuous GPS data, J Geophys Res Solid Earth, 120, 8623–8632, 2015b.

Frederikse, T., Landerer, F., Caron, L., Adhikari, S., Parkes, D., Humphrey, V. W., Dangendorf, S., Hogarth, P., Zanna, L., Cheng, L., and Wu, Y. H.: The causes of sea-level rise since 1900, Nature 2020 584:7821, 584, 393–397, https://doi.org/10.1038/s41586-020-2591-3, 2020.

G. G. Bennett: The calculation of astronomical refraction in marine navigation, The Journal of Navigation, 35, 255–259, 1982.

Gee, M. J. R., Uy, H. S., Warren, J., Morley, C. K., and Lambiase, J. J.: The Brunei slide: A giant submarine landslide on the North West Borneo Margin revealed by 3D seismic data, Mar Geol, 246, 9–23,

https://doi.org/10.5194/egusphere-2025-3563
Preprint. Discussion started: 16 September 2025
© Author(s) 2025. CC BY 4.0 License.

https://doi.org/10.1016/j.margeo.2007.07.009, 2007.

Hamlington, B. D., Bellas-Manley, A., Willis, J. K., Fournier, S., Vinogradova, N., Nerem, R. S., Piecuch, C. G., Thompson, P. R., and Kopp, R.: The rate of global sea level rise doubled during the past three decades, Communications Earth & Environment 2024 5:1, 5, 1–4, https://doi.org/10.1038/s43247-024-01761-5, 2024.

Han, S. C., Ghobadi-Far, K., Yeo, I. Y., McCullough, C. M., Lee, E., and Sauber, J.: GRACE Follow-On revealed Bangladesh was flooded early in the 2020 monsoon season due to premature soil saturation, Proc Natl Acad Sci U S A, 118, e2109086118, https://doi.org/10.1073/PNAS.2109086118/SUPPL_FILE/PNAS.2109086118.SAPP.PDF, 2021.

Hay, C. C., Morrow, E., Kopp, R. E., and Mitrovica, J. X.: Probabilistic reanalysis of twentieth-century sea-level rise, Nature, 517, 481–484, 2015.

Herring, T. A., Melbourne, T. I., Murray, M. H., Floyd, M. A., Szeliga, W. M., King, R. W., Phillips, D. A., Puskas, C. M., Santillan, M., and Wang, L.: Plate Boundary Observatory and related networks: GPS data analysis methods and geodetic products, Reviews of Geophysics, 54, 759–808, 2016.

Hill, E. M., Borrero, J. C., Huang, Z., Qiu, Q., Banerjee, P., Natawidjaja, D. H., Elosegui, P., Fritz, H. M., Suwargadi, B. W., Pranantyo, I. R., Li, L., Macpherson, K. a., Skanavis, V., Synolakis, C. E., and Sieh, K.: The 2010 M w 7.8 Mentawai earthquake: Very shallow source of a rare tsunami earthquake determined from tsunami field survey and near-field GPS data, J Geophys Res, 117, B06402, https://doi.org/10.1029/2012JB009159, 2012.

Horton, B. P., Kopp, R. E., Garner, A. J., Hay, C. C., Khan, N. S., Roy, K., and Shaw, T. A.: Mapping Sea-Level Change in Time, Space, and Probability, Annu Rev Environ Resour, 43, 481–521, https://doi.org/10.1146/annurev-environ-102017-025826, 2018.

Hsu, Y. J., Yu, S. B., Song, T. R. A., and Bacolcol, T.: Plate coupling along the Manila subduction zone between Taiwan and northern Luzon, J Asian Earth Sci, 51, 98–108, https://doi.org/https://doi.org/10.1016/j.jseaes.2012.01.005, 2012.

Hsu, Y. J., Yu, S. B., Loveless, J. P., Bacolcol, T., Solidum, R., Luis Jr, A., Pelicano, A., and Woessner, J.: Interseismic deformation and moment deficit along the Manila subduction zone and the Philippine Fault system, J Geophys Res Solid Earth, 121, 7639–7665, https://doi.org/10.1002/2016JB013082, 2016.

Kanamori, H.: Mechanism of tsunami earthquakes, Physics of the Earth and Planetary Interiors, 6, 346–359, https://doi.org/10.1016/0031-9201(72)90058-1, 1972.

Kawamoto, S., Hiyama, Y., Ohta, Y., and Nishimura, T.: First result from the GEONET real-time analysis system (REGARD): The case of the 2016 Kumamoto earthquakes, Earth, Planets and Space, 68, 1–12, https://doi.org/10.1186/S40623-016-0564-4/TABLES/3, 2016.

Koulali, A., McClusky, S., Cummins, P., and Tregoning, P.: Wedge geometry, frictional properties and

https://doi.org/10.5194/egusphere-2025-3563
Preprint. Discussion started: 16 September 2025
© Author(s) 2025. CC BY 4.0 License.

591 interseismic coupling of the Java megathrust, Tectonophysics, 734–735, 89–95,
592 https://doi.org/10.1016/j.tecto.2018.03.012, 2018.
593 Larson, K. M., Ray, R. D., Nievinski, F. G., and Freymueller, J. T.: The Accidental Tide Gauge: A GPS
594 Reflection Case Study From Kachemak Bay, Alaska, IEEE Geoscience and Remote Sensing Letters, 10,
595 1200–1204, https://doi.org/10.1109/LGRS.2012.2236075, 2013.
596 Larson, K. M., Lay, T., Yamazaki, Y., Cheung, K. F., Ye, L., Williams, S. D. P., and Davis, J. L.: Dynamic
597 sea level variation from GNSS: 2020 Shumagin earthquake tsunami resonance and Hurricane Laura,
598 Geophys Res Lett, 48, e2020GL091378, 2021.
599 Lau, A. Y. A., Switzer, A. D., DomineyHowes, D., Aitchison, J. C., and Zong, Y.: Written records of
600 historical tsunamis in the northeastern South China Sea-challenges associated with developing a new
601 integrated database, Natural Hazards and Earth System Science, 10, 1793--1806,
602 https://doi.org/10.5194/nhess-10-1793-2010, 2010.
603 Lay, T.: The surge of great earthquakes from 2004 to 2014, Earth Planet Sci Lett, 409, 133–146, 2015.
604 Lay, T.: A review of the rupture characteristics of the 2011 Tohoku-oki Mw 9.1 earthquake, Tectonophysics,
605 733, 4–36, https://doi.org/https://doi.org/10.1016/j.tecto.2017.09.022, 2018.
606 Lay, T. and Kanamori, H.: Insights from the great 2011 Japan earthquake, Phys Today, 64, 33–39,
607 https://doi.org/10.1063/PT.3.1361, 2011.
608 Li, C. F., Xu, X., Lin, J., Sun, Z., Zhu, J., Yao, Y., Zhao, X., Liu, Q., Kulhanek, D. K., Wang, J., Song, T.,
609 Zhao, J., Qiu, N., Guan, Y., Zhou, Z., Williams, T., Bao, R., Briais, A., Brown, E. A., Chen, Y., Clift, P. D.,
610 Colwell, F. S., Dadd, K. A., Ding, W., Almeida, I. H., Huang, X. L., Hyun, S., Jiang, T., Koppers, A. A. P.,
611 Li, Q., Liu, C., Liu, Z., Nagai, R. H., Peleo-Alampay, A., Su, X., Tejada, M. L. G., Trinh, H. S., Yeh, Y. C.,
612 Zhang, C., Zhang, F., and Zhang, G. L.: Ages and magnetic structures of the South China Sea constrained
613 by deep tow magnetic surveys and IODP Expedition 349, Geochemistry, Geophysics, Geosystems, 15,
614 4958–4983, https://doi.org/10.1002/2014GC005567, 2014.
615 Li, J., Ding, W., Lin, J., Xu, Y., Kong, F., Li, S., Huang, X., and Zhou, Z.: Dynamic processes of the curved
616 subduction system in Southeast Asia: A review and future perspective, Earth Sci Rev, 217, 103647, 2021.
617 Li, L., Switzer, A. D., Chan, C. H., Wang, Y., Weiss, R., and Qiu, Q.: How heterogeneous coseismic slip
618 affects regional probabilistic tsunami hazard assessment: A case study in the South China Sea, J Geophys
619 Res Solid Earth, 121, 6250– 6272, https://doi.org/10.1002/2016JB013111, 2016.
620 Li, L., Switzer, A. D., Wang, Y., Chan, C. H., Qiu, Q., and Weiss, R.: A modest 0.5-m rise in sea level will
621 double the tsunami hazard in Macau, Sci Adv, 4, https://doi.org/10.1126/sciadv.aat1180, 2018.
622 Li, L., Shi, F., Ma, G., and Qiu, Q.: Tsunamigenic potential of the Baiyun slide complex in the South China
623 Sea, J Geophys Res Solid Earth, 124, 7680–7698, 2019.
624 Li, L., Qiu, Q., Li, Z., and Zhang, P.: Tsunami hazard assessment in the South China Sea: A review of recent

https://doi.org/10.5194/egusphere-2025-3563
Preprint. Discussion started: 16 September 2025
© Author(s) 2025. CC BY 4.0 License.

progress and research gaps, Science China Earth Sciences 2022 65:5, 65, 783–809, https://doi.org/10.1007/S11430-021-9893-8, 2022.

Li, L., Qiu, Q., Ye, M., Peng, D., Hsu, Y. J., Wang, P., Shi, H., Larson, K. M., and Zhang, P.: Island-based GNSS-IR network for tsunami detecting and warning, Coastal Engineering, 190, 104501, https://doi.org/10.1016/J.COASTALENG.2024.104501, 2024.

Loveless, J. P. and Meade, B. J.: Two decades of spatiotemporal variations in subduction zone coupling offshore Japan, Earth Planet Sci Lett, 436, 19–30, https://doi.org/https://doi.org/10.1016/j.epsl.2015.12.033, 2016.

Lyard, F. H., Allain, D. J., Cancet, M., Carrère, L., and Picot, N.: FES2014 global ocean tide atlas: Design and performance, Ocean Science, 17, 615–649, https://doi.org/10.5194/OS-17-615-2021, 2021.

Megawati, K., Shaw, F., Sieh, K., Huang, Z., Wu, T. R., Lin, Y., Tan, S. K., and Pan, T. C.: Tsunami hazard from the subduction megathrust of the South China Sea: Part I. Source characterization and the resulting tsunami, J Asian Earth Sci, 36, 13–20, https://doi.org/10.1016/j.jseaes.2008.11.012, 2009.

Mori, N., Satake, K., Cox, D., Goda, K., Catalan, P. A., Ho, T. C., Imamura, F., Tomiczek, T., Lynett, P., Miyashita, T., Muhari, A., Titov, V., and Wilson, R.: Giant tsunami monitoring, early warning and hazard assessment, Nature Reviews Earth & Environment 2022, 1–16, https://doi.org/10.1038/s43017-022-00327-3, 2022.

Noll, C. E.: The crustal dynamics data information system: A resource to support scientific analysis using space geodesy, Advances in Space Research, 45, 1421–1440, https://doi.org/10.1016/J.ASR.2010.01.018, 2010.

Pan, X., Li, L., Nguyễn, H. P., Wang, D., and Switzer, A. D.: Submarine Landslides in the West Continental Slope of the South China Sea and Their Tsunamigenic Potential, Front Earth Sci (Lausanne), 10, 843173, https://doi.org/10.3389/FEART.2022.843173/BIBTEX, 2022.

Paris, R. and Ulvrova, M.: Tsunamis generated by subaqueous volcanic explosions in Taal Caldera Lake, Philippines, Bull Volcanol, 81, 14, https://doi.org/10.1007/s00445-019-1272-2, 2019.

Paris, R., Switzer, A. D., Belousova, M., Belousov, A., Ontowirjo, B., Whelley, P. L., and Ulvrova, M.: Volcanic tsunami: a review of source mechanisms, past events and hazards in Southeast Asia (Indonesia, Philippines, Papua New Guinea), Natural Hazards, 70, 447–470, https://doi.org/10.1007/s11069-013-0822-8, 2014.

Peng, D., Hill, E. M., Li, L., Switzer, A. D., and Larson, K. M.: Application of GNSS interferometric reflectometry for detecting storm surges, GPS Solutions, 23, 47, https://doi.org/10.1007/s10291-019-0838-y, 2019.

Peng, D., Feng, L., Larson, K. M., and Hill, E. M.: Measuring Coastal Absolute Sea-Level Changes Using GNSS Interferometric Reflectometry, Remote Sens (Basel), 13, 4319, https://doi.org/10.3390/rs13214319,

https://doi.org/10.5194/egusphere-2025-3563
Preprint. Discussion started: 16 September 2025
© Author(s) 2025. CC BY 4.0 License.

2021.

Polet, J. and Kanamori, H.: Shallow subduction zone earthquakes and their tsunamigenic potential, Geophys J Int, 142, 684–702, https://doi.org/10.1046/j.1365-246X.2000.00205.x, 2000.

Qiu, Q. and Barbot, S.: Tsunami excitation in the outer wedge of global subduction zones, Earth Sci Rev, 230, 104054, https://doi.org/https://doi.org/10.1016/j.earscirev.2022.104054, 2022.

Qiu, Q., Li, L., Hsu, Y. J., Wang, Y., Chan, C. H., and Switzer, A. D.: Revised earthquake sources along Manila trench for tsunami hazard assessment in the South China Sea, Natural Hazards and Earth System Sciences, 19, 1565–1583, 2019.

Ramos, N. T., Maxwell, K. V., Tsutsumi, H., Chou, Y. C., Duan, F., Shen, C. C., and Satake, K.: Occurrence of 1 ka-old corals on an uplifted reef terrace in west Luzon, Philippines: Implications for a prehistoric extreme wave event in the South China Sea region, https://doi.org/10.1186/s40562-017-0078-3, 2017.

Roesler, C. and Larson, K. M.: Software tools for GNSS interferometric reflectometry (GNSS-IR), GPS Solutions, 22, 80, https://doi.org/10.1007/s10291-018-0744-8, 2018.

Scherneck, H. G: A parametrized solid earth tide model and ocean tide loading effects for global geodetic baseline measurements, Geophys J Int, 106, 677–694, https://doi.org/10.1111/J.1365-246X.1991.TB06339.X, 1991.

Strandberg, J., Hobiger, T., and Haas, R.: Real-time sea-level monitoring using Kalman filtering of GNSS-R data, GPS Solutions, 23, 61, https://doi.org/10.1007/s10291-019-0851-1, 2019.

Sun, Q., Cartwright, J., Xie, X., Lu, X., Yuan, S., and Chen, C.: Reconstruction of repeated Quaternary slope failures in the northern South China Sea, Mar Geol, 401, 17–35, https://doi.org/https://doi.org/10.1016/j.margeo.2018.04.009, 2018.

Sun, Z., Zhong, Z., Keep, M., Zhou, D., Cai, D., Li, X., Wu, S., and Jiang, J.: 3D analogue modeling of the South China Sea: A discussion on breakup pattern, J Asian Earth Sci, 34, 544–556, https://doi.org/10.1016/J.JSEAES.2008.09.002, 2009.

Sun, Z., Lin, J., Qiu, N., Jian, Z., Wang, P., Pang, X., Zheng, J., and Zhu, B.: The role of magmatism in the thinning and breakup of the South China Sea continental margin: Special Topic: The South China Sea Ocean Drilling, Natl Sci Rev, 6, 871–876, https://doi.org/10.1093/NSR/NWZ116, 2019.

Tapponnier, P., Zhiqin, X., Roger, F., Meyer, B., Arnaud, N., Wittlinger, G., and Jingsui, Y.: Oblique Stepwise Rise and Growth of the Tibet Plateau, Science (1979), 294, 1671–1677, https://doi.org/10.1126/SCIENCE.105978, 2001.

Terry, J. P., Winspear, N., Goff, J., and Tan, P. H. H.: Past and potential tsunami sources in the South China Sea: A brief synthesis, Earth Sci Rev, 167, 47–61, https://doi.org/https://doi.org/10.1016/j.earscirev.2017.02.007, 2017.

Tu, J., Wei, H., Zhang, R., Yang, L., Lv, J., Li, X., Nie, S., Li, P., Wang, Y., and Li, N.: GNSS-IR Snow

https://doi.org/10.5194/egusphere-2025-3563
Preprint. Discussion started: 16 September 2025
© Author(s) 2025. CC BY 4.0 License.

Depth Retrieval from Multi-GNSS and Multi-Frequency Data, Remote Sensing 2021, Vol. 13, Page 4311, 13, 4311, https://doi.org/10.3390/RS13214311, 2021.

Wang, H., Li, W., and Xiang, W.: Sea level rise along China coast in the last 60 years, Acta Oceanologica Sinica 2022 41:12, 41, 18–26, https://doi.org/10.1007/S13131-022-2066-5, 2022.

Wang, K. and Bilek, S. L.: Invited review paper: Fault creep caused by subduction of rough seafloor relief, Tectonophysics, 610, 1–24, https://doi.org/10.1016/j.tecto.2013.11.024, 2014.

Wang, W., Wang, D., Wu, S., Völker, D., Zeng, H., Cai, G., and Li, Q.: Submarine landslides on the north continental slope of the South China Sea, Journal of Ocean University of China, 17, 83–100, https://doi.org/10.1007/S11802-018-3491-0/METRICS, 2018.

Wang, X. and Liu, P. L. F.: An analysis of 2004 Sumatra earthquake fault plane mechanisms and Indian Ocean tsunami, Journal of Hydraulic Research, 44, 147–154, https://doi.org/10.1080/00221686.2006.9521671, 2006.

Wang, X. and Liu, P. L. F.: Numerical Simulations of the 2004 Indian Ocean Tsunamis — Coastal Effects, Journal of Earthquake and Tsunami, 01, 273–297, https://doi.org/10.1142/S179343110700016X, 2007.

Wessel, P., Smith, W. H. F., Scharroo, R., Luis, J., and Wobbe, F.: Generic Mapping Tools: Improved Version Released, Eos, Transactions American Geophysical Union, 94, 409–410, 2013.

Wessel, P., Luis, J. F., Uieda, L., Scharroo, R., Wobbe, F., Smith, W. H. F., and Tian, D.: The generic mapping tools version 6, Geochemistry, Geophysics, Geosystems, 20, 5556–5564, 2019.

Xia, S., Zhou, P., Zhao, D., and Cao, J.: Seismogenic structure in the source zone of the 1918 M7.5 NanAo earthquake in the northern South China Sea, Physics of the Earth and Planetary Interiors, 302, 106472, https://doi.org/10.1016/j.pepi.2020.106472, 2020.

Xu, Z., Liang, S., Abd Rahman, M. N. Bin, Li, H., and Shi, J.: Historical earthquakes, tsunamis and real-time earthquake monitoring for tsunami advisory in the South China Sea region, Natural Hazards, 107, 771–793, https://doi.org/10.1007/S11069-021-04605-Z/FIGURES/10, 2021.

Yang, W. , Sun, L., Yang, Z., Gao, S., Gao, Y., Shao, D., Mei, Y., Zang, J., Wang, Y., and Xie, Z.: Nan'ao, an archaeological site of Song dynasty destroyed by tsunami, Chinese Science Bulletin, 2018.

Yu, K. F., Zhao, J. X., Shi, Q., and Meng, Q. S.: Reconstruction of storm/tsunami records over the last 4000 years using transported coral blocks and lagoon sediments in the southern South China Sea, Quaternary International, 195, 128–137, https://doi.org/https://doi.org/10.1016/j.quaint.2008.05.004, 2009.

Zhao, G. and Niu, X.: Tsunami hazard assessment in the South China Sea based on geodetic locking of the Manila subduction zone, Natural Hazards and Earth System Sciences, 24, 2303–2313, https://doi.org/10.5194/NHESS-24-2303-2024, 2024.

Zhu, Y., An, C., Yu, H., Zhang, W., and Chen, X.: High-resolution tsunami hazard assessment for the Guangdong-Hong Kong-Macao Greater Bay Area based on a non-hydrostatic tsunami model, Sci China

https://doi.org/10.5194/egusphere-2025-3563
Preprint. Discussion started: 16 September 2025
© Author(s) 2025. CC BY 4.0 License.

727 Earth Sci, 67, 2326–2351, https://doi.org/10.1007/S11430-023-1300-9/METRICS, 2024.
728 Zorn, E. U., Orynbaikyzy, A., Plank, S., Babeyko, A., Darmawan, H., Robbany, I. F., and Walter, T. R.:
729 Identification and ranking of subaerial volcanic tsunami hazard sources in Southeast Asia, Natural Hazards
730 and Earth System Sciences, 22, 3083–3104, https://doi.org/10.5194/NHESS-22-3083-2022, 2022.
731